Department of physics, École Normale Supérieure, Paris

NITROGEN VACANCIES IN DIAMOND

Report Experimental Physics

Bryan Gerard, Andrea Combette

Cautionary note : We inform the reader that this document is not an article but a report, and thus also aims at describing the whole path to the results, including experimental errors and wrongful intuitions. The first part provides theoretical considerations on the subject that are required for understanding the results. The following parts focus more precisely on the experimental aspects, stressing the difficulties encountered and their solutions.

Contents

I Introduction **2**

II General properties of the Nitrogen-Vacancy color center **2**

1 Diamond structure and synthesis . . . 2
2 Electronic structure and optical properties . . . 3
3 Spin properties and Zeeman effect . . . 4

III Experimental demonstration **5**

1 Aim of the experiment . . . 5
2 Experimental setup . . . 6
a Rise-time of the AOM and RF propagation . . . 6
b Generation of the RF-signal with amplitude modulation . . . 7
c Choice of internal modulation . . . 7
d Burst Mode . . . 8
d.1 Principle . . . 8
d.2 Pros . . . 8
e Rise-time of the photodiode . . . 8
f Table of characteristic time . . . 8
g Experimental Setup. . . . 9

IV Results & Analyses **9**

1 Excitation timescale . . . 9
a Probability of the transition **metastable** $\longrightarrow |0\rangle_g$ . . . 10
b Expomential Truncation . . . 10
2 Relaxation timescale . . . 11
3 Zeeman Effet . . . 11
a Spectrum without any externally applied magnetic field . . . 12
b Spectrum with external magnetic field . . . 13
c Exploitation of the Zeeman effect . . . 13
c.1 Data exploration . . . 13
c.2 Projections in a tetrahedron . . . 15
c.3 Frequency split distribution study . . . 15
c.4 Results . . . 16

V Conclusion and Prospectus **17**

I Introduction

Diamond properties have been studied all over by physicists who took advantage of the material's heat conductivity, mechanical hardness and optical transparency. The diamond lattice is constituted by carbon atoms, regularly distributed in space according to the diamond cubic crystal structure. Nonetheless, this regularity is frequently transgressed and one or many carbon atoms jump out of the lattice structure, creating defects. Either filled or not, these defects can thus be vacant lattice site or even replaced by impurity atoms. Even though diamond is optically transparent, impurities in the structure can change its optical properties by creating fluorescent lattice defects that are called "Color centers".

Color centers are responsible for the typical coloration of diamond gemstones. Physicists have already identified several hundred defects by their optical emission and absorption spectra. The most interesting properties of these centers are their sub-nanometric size and their high stability and sensitivity, even in nanometre-size cristals, making them ideal candidates for high-resolution local probes.

The color center studied in this paper is the "Nitrogen-Vacancy Center" (NV-center), consisting in two neighboring lattice defects replaced by one Nitrogen atom and a vacancy. The reason for this lies in its magnetic and quantum properties up to room temperature. Combined with the pysicists' ability to control electronic properties of single impurities, NV-center are the basis of many quantum manipulation protocols [3] such as the electron paramagnetic resonance (EPR) [2]. The detection of EPR from a single NV defect opens the way to a wide variety of applications in nanoscale-resolution sensing of magnetic fields near superconductors, spin textures or spintronic devices for example. In biological field, NV centers are also used as fluorescent biomarkers [1].

Besides, recent evidence of quantum teleportation and entanglement has put the emerging quantum technologies in the spotlight, with the eternal dream of creating a quantum computer, that would be able to solve currently numerically unsolvable problems. This evolution had shed light on the quantum processing units, usually called 'qubits' (short for 'quantum bits'). There are nowadays five main ways of creating such qubits, one of them is using the quantum properties of NV centers [4].

This reports aims at describing the properties of these so-called "NV-centers" (NV short for Nitrogen-Vacancy) and their manipulation through optical pumping. A second part will address the Zeeman effect on a NV-Center submitted to microwaves with an externally applied magnetic field.

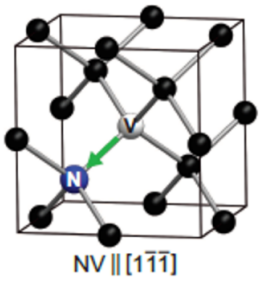

Figure 1: NV Center inside a diamond crystal, composed of one nitrogen atom (N) (blue) and one vacancy (V) (white) located on neighboring sites.

II General properties of the Nitrogen-Vacancy color center

1 Diamond structure and synthesis

Nitrogen-Vacancy center (NV-centers) are vacancies inside a diamond lattice, in which two neighboring sites of the initial carbon lattice are empty, and one of them is filled by a Nitrogen atom. This atom is then 'trapped' in the lattice. Even though natural diamonds contain a certain number of NV centers, there is typically of 1 out of 1000 nanometre-size commercial samples that host NV centers. Thus their

concentration may be insufficient for some applications. Besides, synthesis processes are reasonably accessible and allow for a precise control of the rates of lattice defaults. A two-step scheme is the following: First, high-energy ion or electron irradiation creates a lot of vacancy in the host structre, then high-temperature annealing ($\leq 800\ °C$) promotes the formation of NV centers through vacancy diffusion. This process allows for a few NV centers in a 10-nm particle and a nitrogen to NV conversion of the order of 10%.

2 Electronic structure and optical properties

The electronic structure of the NV center involves six electrons. Two of them are provided from the nitrogen atom, three other by the neighboring carbons and the last one is captured from the lattice, making the color center negatively charged, usually denoted NV^-.

Since there are many energies available to the trapped nitrogen atom, this is possible to control its states. Hence, the Nitrogen-Vacancy-centers are one of the five main ways to create a single unit of quantum processing, usually called qubit. A schematic energy-level diagram of the NV center is shown in Fig.2. The basic description of the photophysics involve only three electronic levels, the ground state denoted $|\cdot\rangle_g$, the excited state $|\cdot\rangle_e$ and a metastable state $|\cdot\rangle_m$.

Both excited and ground states are spin triplets ($S = 1$) while metastable state is a singlet ($S = 0$). The two triplet states (ground and excited states) are split into three sublevels. The energy levels will thus be denoted $|0\rangle_.$ ($m_s = 0$) of energy E_{0g} and $|1\rangle_.$ ($m_s = \pm 1$) of energy E_{1g}, with $E_{0g} < E_{1g}$. The NV-centers can reach excited states through non-resonant laser excitation with $\lambda_{laser} = 532\ nm$ (green laser):

$$|0\rangle_g \xrightarrow{\lambda_{laser}=532nm} |0\rangle_e \qquad\qquad |1\rangle_g \xrightarrow{\lambda_{laser}=532nm} |1\rangle_e$$

Without any externally applied magnetic field, $|1\rangle_{g/e}$ describes two degenerate states in both ground and excited states. The degeneracy of these sublevels results from the axial symmetry of the NV center.

For NV-centers in the initial state $|0\rangle_g$, the laser excitation first bring the system in the intermediate state $|0\rangle'_e$. After a quick phononic (non radiative) relaxation (sub-ns process), the system reaches the excited system $|0\rangle_e$, before relaxing to the state $|0\rangle_g$ by emitting one red photon of wavelength $\lambda = 638\ nm$. This 3-step relaxation process has a typical timescale of 10 ns, much lower that the resolution of our measuring devices, so we won't focus on it. In the following, we will only consider that the initial ground state $|0\rangle_g$ reaches the excited state $|0\rangle_e$ by absorbing a green photon, and instantly relaxes to its initial state by emitting a red one (the energy conservation is not satisfied in this model, but since we won't go in the details of it, this won't matter for the following).

$$|0\rangle_g \underset{\lambda_{emission}=638nm}{\overset{\lambda_{laser}=532nm}{\rightleftharpoons}} |0\rangle_e \qquad\qquad |1\rangle_g \underset{\lambda_{emission}=638nm}{\overset{\lambda_{laser}=532nm}{\rightleftharpoons}} |1\rangle_e$$

Regarding the NV-centers initially occupying the state $|1\rangle_g$, the excitation-relaxation process is a bit more complicated. For clarity purposes, we will only describe its dynamics schematically. A more detailed description is available in [5]. Let us consider NV-centers initially in $|1\rangle_g$. The green laser will excite them to the higher energetic state $|1\rangle'_e$. The NV-center will then relax (comparably to the state $|0\rangle$ through non-radiative phononic emission) to the excited state $|1\rangle_e$. There are two possible ways of relaxing for NV electrons in $|1\rangle_e$. Either the electron relaxes directly to $|1\rangle_g$ via the same process as the one described above, or via a metastable state. The radiative triplet-triplet transition (first path) is the most favorable one (probability of 0.7-0.8) and is dependant of the spin state. The non-radiative transition involves a metastable state $|1\rangle_m$ of energy E_{1m}, such that $E_{1e} - E_{1m} \approx E_{1m} - E_{1g}$. The electron then relaxes preferentially to $|0\rangle_g$. Since the transitions $|1\rangle_g \longrightarrow |1\rangle_g$ and $|1\rangle_g \longrightarrow |0\rangle_g$ have a lower energy, they are not visible transitions. This 4-step process has a typical timescale of 200 ns, which we will discuss in the following. These processes are recapitulated in Fig.2.

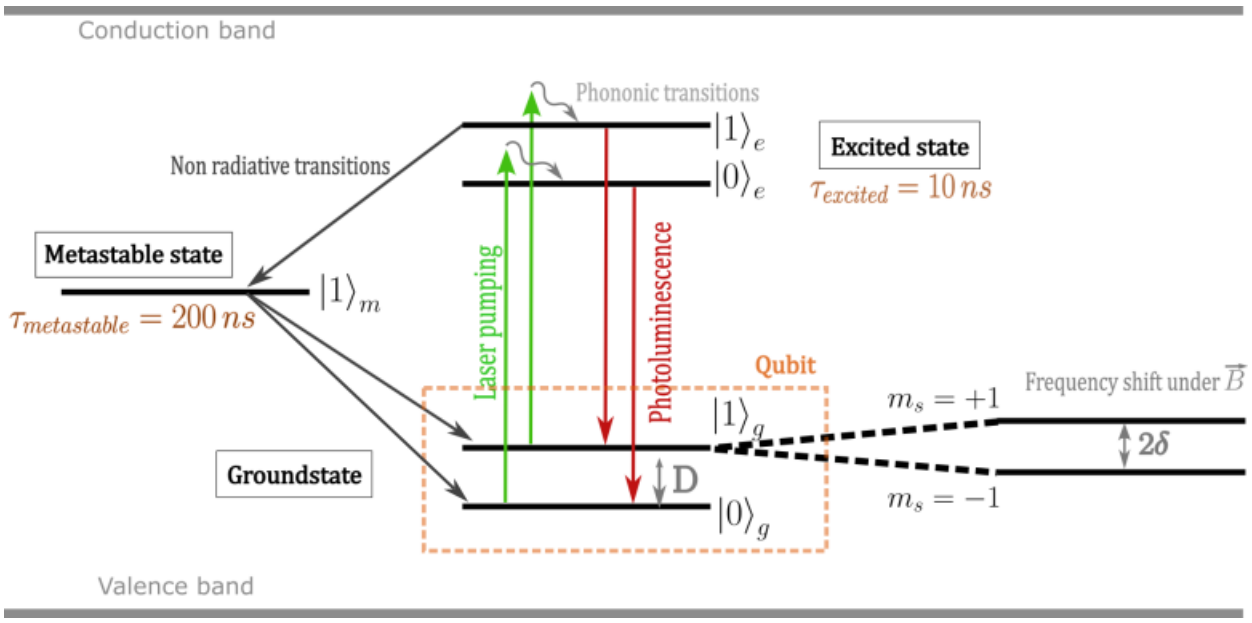

Figure 2: Energy-level diagram of the NV-center. $|\cdot\rangle_g$ denotes the electronic ground state, $|\cdot\rangle_e$ the electronic excited state, $|\cdot\rangle_m$ the metastable state. Green and red straight arrows indicate radiative transitions, straight dark grey arrows the strong nonradiative decay via the metastable state, light gray wiggly arrows the phonoic transitions in the crystal.

Hence, if we consider an initial state with a proportion x_0 of NV-centers in the state $|0\rangle_g$, and $x_1 = 1 - x_0$ ones in the state $|1\rangle_g$, we typically have at the end of one cycle (ie. if we consider illuminating our sample with pulse of infinitesimal duration of wavelength λ_{laser} and if every electron is irradiated) a proportion $0.7 \times x_1$ center in the state $|1\rangle_g$ and $x_0 + 0.3 \times x_1$ centers in the state $|0\rangle_g$. After only a few cycles, we can consider that every NV center is in the $|0\rangle$ state. The real processes are actually much more complicated than the described one and there will always subsist a fraction of NV in $|1\rangle$ states, but this provides a good schematic idea of the considered dynamics of the material.

3 Spin properties and Zeeman effect

The special features of NV centers are that they have nonzero spin and thus show magnetic behaviour up to room temperature. The luminescence of these particular color centers is coupled to the spin state, such that the luminescence intensity can be modulated by magnetic fields. Only few other color centers exhibit such properties. Hence, NV-centers can be manipulated by applying an external electromagnetic field on the diamond sample through Zeeman effect.

Without externally applied magnetic field, the energy difference between spin sublevels is $D = 2.87\ GHz$ for the ground state and $D' = 1.42\ GHz$ for the excited state. D is the zero-field splitting, described in [5]. The transition between spin sublevels $|0\rangle_{g/e}$ and $|1\rangle_{g/e}$ (ie. between $m_s = 0$ and $m_s = \pm 1$) is given by the spin-lattice relaxation time and is a few milliseconds at room temperature. The triplet-triplet transitions are also strongly spin preserving (ie. the spin state does not change while transitioning between excited and ground state $|\cdot\rangle_g \longleftrightarrow |\cdot\rangle_e$). The $|0\rangle_g$ state corresponds to $m_s = 0$ while the $|1\rangle_{g\pm1}$ states correspond to $m_s = \pm 1$.

The presence of an external magnetic field changes the dynamics of the problem. The interaction between the NV spin and the external field B can be expressed using the following spin Hamiltonian [5]:

$$\mathcal{H} = hDS_z^2 + hE(S_x^2 - S_y^2) + g\mu_B \vec{B}.\vec{S} \tag{1}$$

Here D and E are the zero-field splitting parameter (not to be confused with the electric field whose interaction with the NV center is neglected here), that expressed the small energy gap between the

two sublevels $|1\rangle_{g\pm1}$ for $B = 0$. Then let's assume that $B_\perp \ll hd/g\mu_b$ (this consideration on the transversal component of $\vec{B}$ is valid in weak magnetic field regime). Then, when we apply a magnetic field $\vec{B}$, the Hamiltonian's eigenvalues become :

$$\nu_\pm = D \pm \sqrt{(\frac{g\mu_B}{h}B_{NV})^2 + E^2} \tag{2}$$

where B_{NV} is the projection of B on the NV center axis denoted z in (1). We will denote in the following $\delta = \sqrt{(\frac{g\mu_B}{h}B_{NV})^2 + E^2} > 0$.

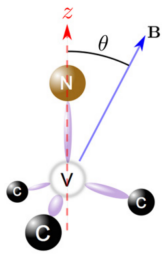

Figure 3: Schematic of the NV-axis and the external magnetic field $\vec{B}$.

On the schematic of Fig.3, we see that given the crystal structure of diamond, called diamond cubic, there are only 4 possibilities for the NV-axis (axis that goes through the vacancy and the nitrogen atom). Given that diamond has a periodic crystal structure, we can extend this observation to our macroscopic sample and state that there are overall only 4 different defects axis.

Hence, in presence of an external magnetic field, the two degenerate sub-levels $|1\rangle_g$ with $m_s = 1$ and $m_s = -1$ will split into two non-degenerate sub-levels $|1\rangle_{g,m_s=-1}$ and $|1\rangle_{g,m_s=+1}$ of quasi-similar energies $E_{g,m_s=-1}$ and $E_{g,m=s+1}$ respectively. This shift of energy sublevels will change the resonance frequency of the microwave transition $|0\rangle_g \to |1\rangle_g$, which was initially $D = 2.87\,GHz$. According to quantum mechanics, there will thus be two different transitions, with two different resonant frequencies, centered in D, $D + \delta$ and $D - \delta$ for the transitions $|0\rangle_g \to |1\rangle_{g,+1}$ and $|0\rangle_g \to |1\rangle_{g,-1}$ respectively. For example, sending a microwave of frequency $D + \delta$ in the diamond will enhance the transition $|0\rangle_g \to |1\rangle_{g,+1}$ and not the $|0\rangle_g \to |1\rangle_{g,-1}$.

This interesting property can be easily exploited. If we wait long enough (a few milliseconds as mentioned in part II.3) while pumping with the green laser, only the $|0\rangle_{g/e}$ will be populated. Sending a microwave at frequency $D + \delta$ or $D - \delta$ would then change the proportions of $|0\rangle_g$ and $|1\rangle_{g\pm1}$ (ie. increase the one of $|1\rangle_{g/e,\pm1}$), thus changing the luminescence intensity of the sample. Sending a frequency-sweep for example would thus change the luminescence intensity only as the microwave-frequency gets closer to $D - \delta$ and $D + \delta$, consisting an evidence of Zeeman effect.

III Experimental demonstration

1 Aim of the experiment

The aim of the conducted experiment that is described in this report is to properly understand and image the energy-transitions depicted in the previous paragraphs.

The first step is to build the experimental setup and to align the different optics. This will enable us to evaluate the different timescales of excitation and relaxation of the system. These are different from the timescales of a unique excitation/relaxation mentioned in part II given that every single process is probabilistic and that a macroscopic behavior is much more complex that an isolated one. This will necessitate the use of an Acousto-Optic Modulator (AOM) which will enable to deviate (and thus obtrude) the laser beam in a very short range of time, allowing precise time measurements. By observing the evolution of the luminescence intensity (ie. red light emerging from the laser-irradiated

diamond), we can thus draw conclusions on the dynamics of the NV-centers. The experimental manipulations consist in placing an AOM on the green laser beam trajectory, in aligning the optics in order to keep only the deviated green-laser beam (ie. the non-zero terms of the AOM) to focus on the sample, and in conjugating the diamond with a photodiode to observe its (red-)luminescence.

The second step of the experiment is then to highlight Zeeman effect by manipulating the energy levels of the NV-centers through an externally applied magnetic field. The shift of EPR frequencies can be imaged simply by recording the evolution of the luminescence intensity of the diamond sample under microwave perturbation. This informs on the quantum mechanics of the Zeeman effect in general, and also on the nature of the different states observed. Our goal will be to show that there appears resonant frequencies centered in $D = 2.87\ GHz$, and to try to manipulate them as much as possible.

2 Experimental setup

The experimental setup is depicted in figure 6.

We use a green laser of wavelength $\lambda = 532\ nm$ from Thorlabs. The laser beam diameter of around ten millimeters is first reduced with a telescope magnification $\Delta = -4$ created by two converging lenses with focal lengths 20 cm for the first one and 5 cm for the second one, distant from 25 cm from each other. The laser beam is then directed on an Acousto-Optic Modulator (AOM) form Thorlabs. The reducing of beam diameter is an essential aspect of the experimental setup. The laser is then reflected on a dichroic mirror and focused on our diamond sample with a $\times 20$ microscope objective. The sample is fixed on a plane surface bound to a specific moving support, enabling us to control with high precision the five degrees of freedom of our sample (three degrees of position, two degrees of rotation). The green laser beam is sent to infinity before entering the microscope objective. Focusing it on the sample means that the sample is conjugated with the objective which can be equated to a converging lense of very short focal length. Hence, the luminescence of the sample (outgoing red light from the sample) is then sent to infinity with the objective and follows the exact same path as the green laser beam but in the opposite direction. The trajectory of the red light is thus the reversed one of the green light, except that the red light is not reflected by the dichroic mirror and goes through, given that the dichroic mirror acts as a low-pass filter of cut-off wavelength 638 nm. Thanks to the dichroic mirror reflecting green light but transparent for red light, we can then separate the two beams. The luminescence beam is then focused with a converging lense on a photodiode of Thorlabs, covered by a green filter at wavelength 533 nm, in order to measure its intensity.

a Rise-time of the AOM and RF propagation

The rise time of the AOM is a direct consequence of travelling waves inside the crystal. Indeed, to deflect the beam trajectory the RF wave must travel a distance corresponding to the beam diameter, which take a specific time :

$$\tau_{RF} = \frac{d}{c}$$

where d is the beam diameter and c the sound wave velocity in the crystals. A small diameter of the incoming laser beam then increases the efficiency of the AOM. Thus, the timescale of the deviation of the laser beam by the AOM scales with the diameter of the incoming laser beam, which explains the necessity of building a telescope before the AOM.

The AOM is constituted by $Te0_2$ crystals crystals, whose orientations under some stress induced by radiofrequency waves change. It induces a variation of refraction index resulting in a various deviation of light that is completely under the control of the experimenter sending the RF-waves. The AOM uses radiofrequency sinusoidal waves of frequency of the order of $50\,MHz$ to deviate light. This particular system enables one to control with a high time resolution the deviation of light with only a classical Arbitrary Waveform Generator. By obtruding the non-deviated trajectory, one let only the non-zero orders go through, which makes it very easy to control the irradiation of the sample. When one sends radiofrequency waves into the AOM, the device deviates light and luminescence is observed

from the diamond sample, when no signal is sent into the AOM, then light is not deviated, and only the obtruded zero-order exists, thus no luminescence can be observed. Hence, the AOM device allows us to have a time resolved irradiation of our sample.

The data sheet of the AOM used in the experiment gives us an approximate range of values of the input power to maximize the efficiency of deviation. The input power should be around $1\,W$.

b Generation of the RF-signal with amplitude modulation

In order to have a precise control of our AOM, we use an amplitude-modulated sinusoidal signal of frequency of $f_{signal} = 50\,MHz$ and amplitude $6.4\,Vpp$ thus $3.2\,V$ generated by an Arbitrary Waveform Generator coupled to a RF-amplifier. The measured output resistance of the generator is $48.7\,\Omega$ This produces an outpower from the generator of $P_{out} = \frac{U^2}{2R} = 0.1W$. The signal is then transmitted to an amplifier of gain $20\,dB$ which makes the input power in the AOM to $P_{out} = 10 \times P_{in} = 1\,W$.

The ideal modulation signal consists in a square signal with two levels : $1\,V$ during a controlled time T_1 and $0\,V$ during another controlled time T_2, with $T_{1/2}$ going from the tenth of microsecond to tens of seconds. The smaller $T_{1/2}$ can be, the more resolved the measure.

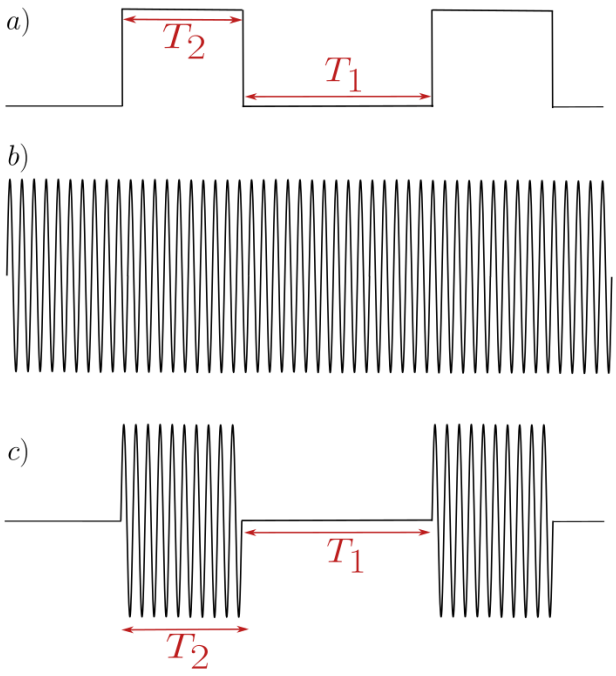

Figure 4: Schematic of the signal used in amplitude modulation. *a)* Amplitude modulation signal. Times T_1 and T_2 are controlled by the experimenter. *b)* RF-signal generetard by RF generator. *c)* Modulated signal sent into the AOM, with controlled T_1 and T_2 times.

c Choice of internal modulation

The choice of the modulation represented an important part of the project. Both internal and external modulations showed advantages and limits. We finally chose the internal modulation (requiring only one generator). In the following we try to focus on our road-map to this conclusion and the difficulties encountered.

We first tried with the internal modulation mode of the generator without succeeding. The reasons were manifold at that time, but the main problem was that the final output was impossible to trigger on. Thus, it was impossible to observe the red light signal obtained with the photodiode on the oscilloscope. A first idea to bypass this problem was to use the external trigger on the oscilloscope instead of the internal trigger mode. This failed because the external trigger signal (which was an

output of the generator) had not the right shape, namely regularly spaced pulses with the frequency of the modulation signal.
Then we tried the external modulation. For this, we used a second generator which aimed at generating the square signal that would consist in the modulation signal. By plugging it into the first generator creating the MHz-frequency sinusoidal signal, the final output should have the right form. Unfortunately it failed mainly due to the long rise time of the amplitude modulation. The result was an amplitude modulation of the form of a trapeze instead of a square (meaning that the rise time wasn't discontinuous as in the square signal but had a finite slope).

d Burst Mode

d.1 Principle The burst mode of a function generator provides a flexible and convenient way to generate short bursts of waveform signals with precise control over parameters such as amplitude, frequency, and duration of cycles. These capabilities makes it essential in our study.

d.2 Pros For relaxation and excitation study, the burst mode is perfect, since it allows us to study a precise time ranges, by tweaking the number of cycles and their durations.

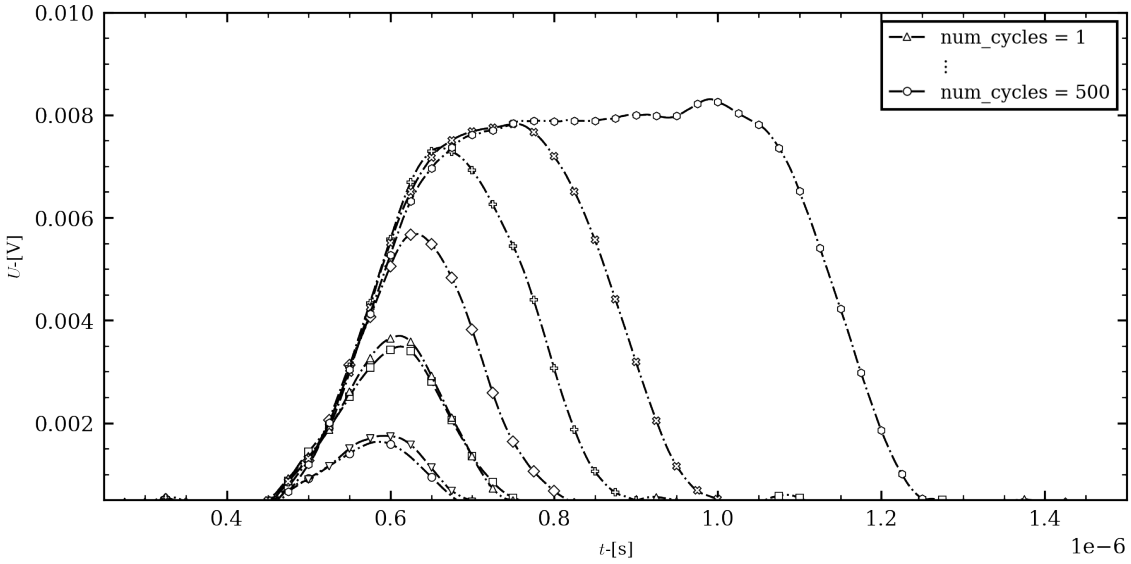

Figure 5: Response of the NV-centers to the green laser exposition. Here we are tweaking the number of cycles of the burst mode. It allows us to control the exposition time of the sample to the green laser, and thus to control the number of metastable cycle between the state $|1\rangle_e$ and the state $|1\rangle_g$. Logically when the exposition time increases the NV-centers response is stronger, leading to an exponential rising behavior. Note that the relaxation time seems to be of the same order as the excitation specific time. Another great point is the ability to control the burst length which, combined with a convenient choice of the number of cycles, allows us to evaluate the time of relaxation of the NV-centers. []

e Rise-time of the photodiode

We measured the rise-time of the photodiode thanks to the AOM. The time-resolved AOM enabled us to measure a rise-time of the order of ten nanoseconds. By fitting the plot with an exponential function, we get exactly $\tau_{PD} = 15\ ns$. This value is smaller than the measures obtained by orders of magnitude so we will neglect the rise-time of the photodiode in the following.

f Table of characteristic time

Characteristics risetimes are given in the following table.

Characteristic times				
τ_{met}	τ_e	τ_{th}	τ_{RF}	τ_{PD}
$\sim$ 200 ns	$\sim$ 13 ns	$\sim$ 300 ns	$\sim$ 100 ns	$\sim$ 15 ns

Table 1: τ_{met}: Metastable path,τ_e: Excitation path, τ_{th}: ,τ_{RF}: Radiofrequency, τ_{PD}: Photodiode., τ_{th} : thermal relaxation

g Experimental Setup.

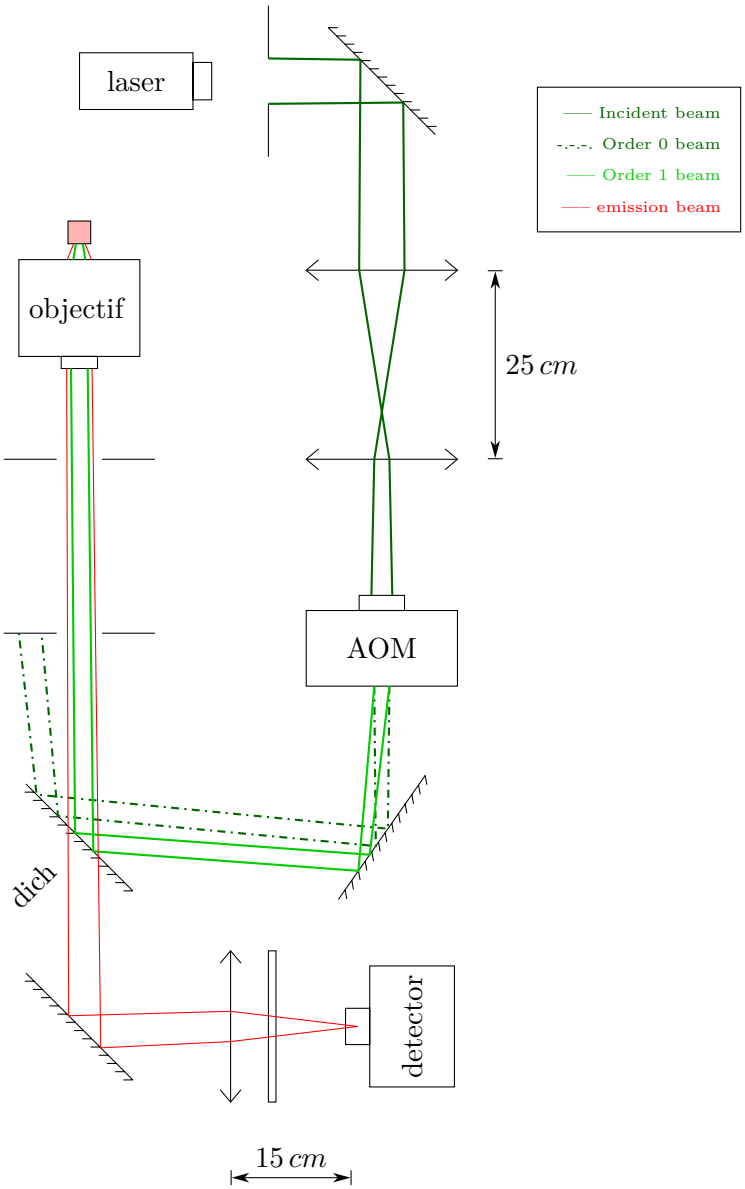

Figure 6: Schematic diagram of the experimental setup and the beam trajectory.

IV Results & Analyses

1 Excitation timescale

The first goal of our study was to study the non-radiative transitions of NV-centers, and to characterize the specific time of this process. Let's recall that the non-radiative transitions determined the radiative timescale since it's the slowest process of the chain ($\tau_{met} \sim 200$ ns). The observation of the diamond

luminescence leads to a succession of saturated exponential. However, multiple timescales are involved in this process, indeed, our experimental setup with the AOM and the photodiode, has its own specific time. Hence, the exploitation of the exponential signal is not a simple task and requires a careful analysis of the different timescales involved.

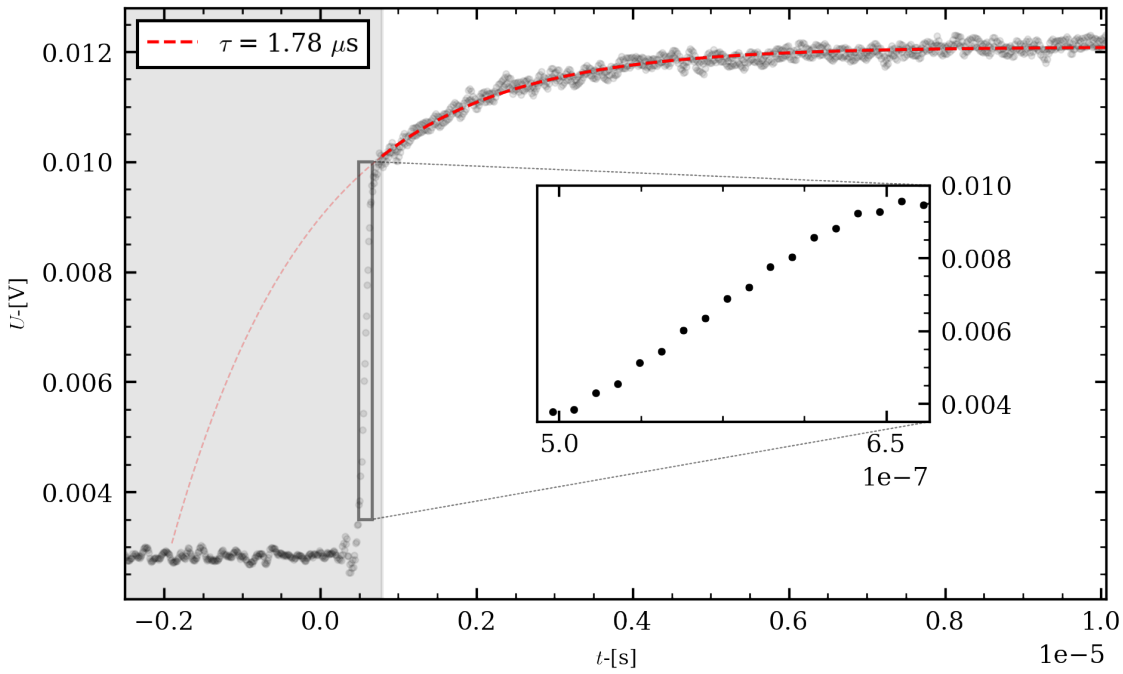

Figure 7: The rising exponential has a characteristic time of $\tau = 1.7 \pm 0.1\,\mu s$. Which is about 10 times the characteristic time of the non-radiative transition for one NV-centers. This is mainly due to the fact that only the $|0\rangle_e$ participate actively in the radiation process, since the $|1\rangle_e$ is involved in the non-radiative transitions. Hence, the exponential rising is pondered by the probability of the transitions **metastable** $\longrightarrow |0\rangle_g$. Furthermore, let's note that the exponential rising must be truncated since the $|0\rangle$ is always populated. The red dotted curve stands for the exponential rising fit of the luminescence. The black framed inset axis is a zoom on the rise due to the AOM and the photodiode, indeed we have a second rise time of $\sim 100\ ns$ which corresponds exactly to the rise-time of the AOM, the photodiode impact is negligible since its rising time is about 10 times smaller than the AOM one.

a Probability of the transition metastable $\longrightarrow |0\rangle_g$

Let's get back on the probability transition of **metastable** $\longrightarrow |0\rangle_g$. We simply got :

$$N(|0\rangle, t)_{|1\rangle} \approx N(|1\rangle, t=0)(1-q)^{\frac{t}{\tau}}$$

Where $N(|0\rangle, t)_{|1\rangle}$ is the number of NV-centers in the state $|0\rangle$ at time t that were in the state $|1\rangle$ at time $t = 0$. And q the conjugated probability of the transition **metastable** $\longrightarrow |0\rangle_g$. This gives us the following approximation with the following assumption $q \ll 1$:

$$N(|0\rangle, t)_{|1\rangle} \approx N(|1\rangle, t=0)e^{-q\frac{t}{\tau}}$$

Hence we got the following apparent transition timescale : $\tau' = \frac{\tau}{q} = 10\tau$. This leads to : $q = 0.1$ and $p = 0.9$. These values are just a rough estimation, since we don't know the exact true value of the rising time.

b Expomential Truncation

The exponential truncation has multiple sources : it's clear that when we excite the sample, all the $|0\rangle$ population will radiate in red, hence when the laser is turned on, the luminescence is already quite

high $\approx \frac{5}{6} I_{\max}$, which is also a good insight of the population rate of $|0\rangle_g$ and $|1\rangle_g$. Indeed, it means that we have approximately $\frac{5}{6}$ of the NV-centers in the $|0\rangle_g$ state at rest. One can show that, thermal relaxation plays also a great role in the exponential truncation, indeed, if the sample is excited with a period less than the thermal relaxation time, the truncation will be greater.

2 Relaxation timescale

To study the thermal relaxation timescale, we take advantage of the burst mode. Indeed playing with the number of cycles and the length of the burst allows us to control precisely the exposition time of the diamond sample. Thanks to that, we can vary the time between two expositions over a short range of time. This short range of time is called σ and is chosen to be the distance between the mid of the rising and decaying exponential. Then we take the mean value of the signal over this short window of time, normally the more σ is important the less the mean value, resulting in an exponential decay.

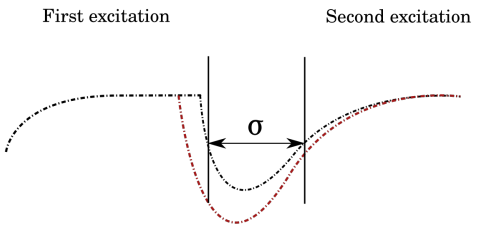

(a) Method for relaxation time measurement

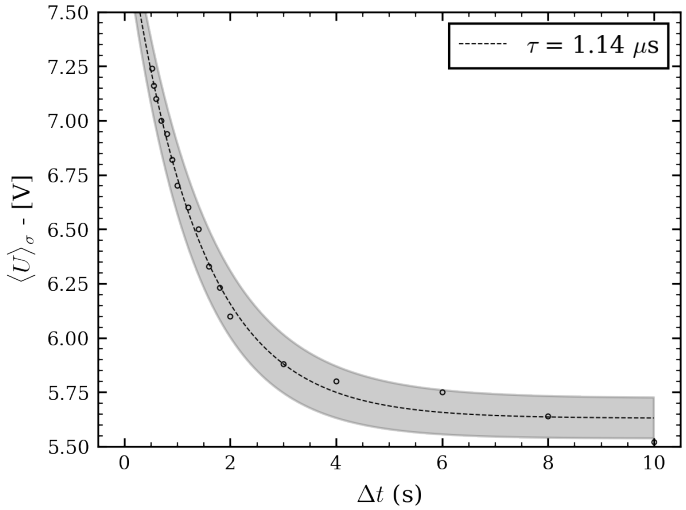

(b) Relaxation time measurement. The relaxation time is about $\tau_{th} = 1.1 \pm .1\,\mu s$.

The relaxation time is about 1 μs which is 300 less than the measured relaxation time by [6]. This huge difference could be explained by the presence of specific salt in the diamond or by collective effect of the NV-centers.[]

3 Zeeman Effet

To begin with, let us consider our diamond sample without any externally applied magnetic field, as in the previous part. We saw in the theoretical considerations of the first part, that energy levels $|1\rangle_{g,m_s=-1}$ and $|1\rangle_{g,m_s=+1}$ were degenerated sub-levels, whereas they are actually non-degenerate with very close energies. Thus, radiofrequency transitions from $|0\rangle_g$ to $|1\rangle_{g,m_s=\pm1}$ have 2 different frequencies. If we denote D the center of these two frequencies and δ the residual frequency shift, we have then two possible transitions:

$$|0\rangle_g \xrightarrow{D-\delta} |1\rangle_{g,m_s=-1} \qquad\qquad |0\rangle_g \xrightarrow{D+\delta} |1\rangle_{g,m_s=+1}$$

with $\delta \ll D$. Since transitions around D have huge timescales, of the order of the millisecond (see part II), this little splitting has no influence on the previous phenomena. Nonetheless, when we prepare our sample in the $|0\rangle$ state through optical pumping, our state can be driven to the states $|1\rangle_{m_s=\pm1}$ by applying a resonant microwave (MW) field. According to the electronic dynamics of the NV defects, there will be a non-negligible fraction of these NV center in the metastable state under laser excitation. Given that the metastable path is (at optical wavelength) non-radiative, these defects won't emit red photons like the defects in the $|0\rangle$ state. This will induce a drop in the luminescence intensity of our

sample. To image this splitting, we want to send radiofrequency (RF) microwaves into our sample close to the frequency D. For this, we build a small metallic loop from a stripped coax cable at the end of which we apply a potential difference which causes a current to appear in the loop. If the loop is small and the cable stripped, there appears a tiny region around the metallic wire where a RF field could exist. To control this RF field, we used a APSYN 420 device from Anapico directly controllable with its software Anapico signal generator gui. We then put the loop close to the sample in order to add our microwave perturbation.

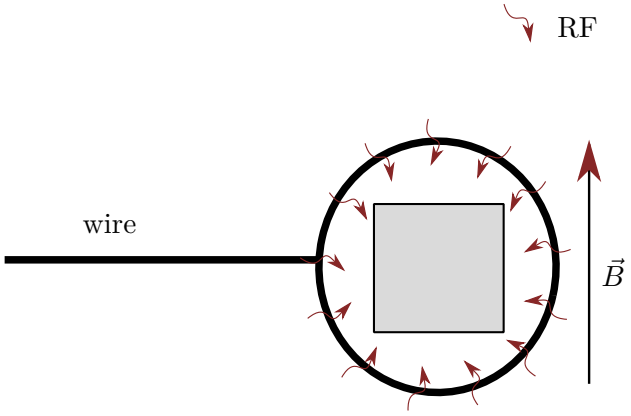

Figure 9: Schematic of the metallic loop used to send RF-microwaves into the diamond sample, in order to alterate the population of the $|1\rangle_g$ state.

a Spectrum without any externally applied magnetic field

Since we know that the transition $|0\rangle_g \leftrightarrow |1\rangle_g$ occurs at $D = 2.87\ GHz$, we vary the frequency thanks to a *swipe* centered in D. Theoretically, the radiation intensity of the diamond should decrease when $D \pm \delta$ is reach since we are populating the $|1\rangle_g$ state (regardless from the spin), hence the $|0\rangle$ red radiation will decrease. In the following we will study the absorbance, and not the emission.

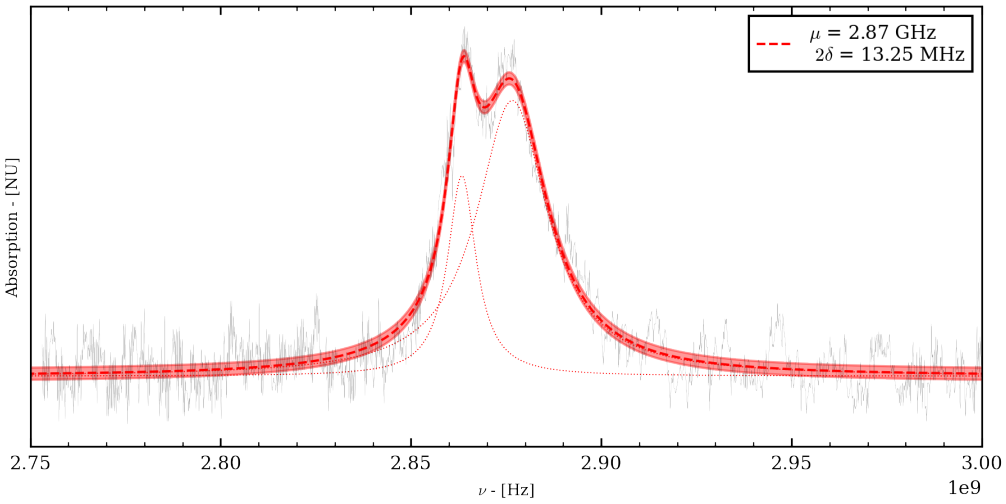

Figure 10: Spectrum recorded without any externally applied field, in red the Lorentzian fit and in black the raw signal. There are two resonant frequencies equally distant from D without any external magnetic field, This highlights the fine energy levels splitting of $|1\rangle_{g,m_s=-1}$ and $|1\rangle_{g,m_s=+1}$ without any external field, this spectrum is not a typical ESR (electron spin resonance), indeed, it unearths the default split in frequency 2δ (2) from the inherent magnetic field. We can approximate $2\delta \approx 13 \pm 1\,MHz$, which means $\delta \approx 6 \pm 1\,MHz$. Rondin et al. in [5] give an approximate value of δ of 5 MHz, which is very close to our value.

b Spectrum with external magnetic field

Let us now vary the external magnetic field applied to our sample. As we saw in II fig.3, Zeeman effect informs us on the degeneracy lifting of the two sublevels $|1\rangle_{g,m_s=-1}$ and $|1\rangle_{g,m_s=+1}$ of a frequency $\delta(\mathbf{B})$ that depends on the magnetic field $\mathbf{B}$.

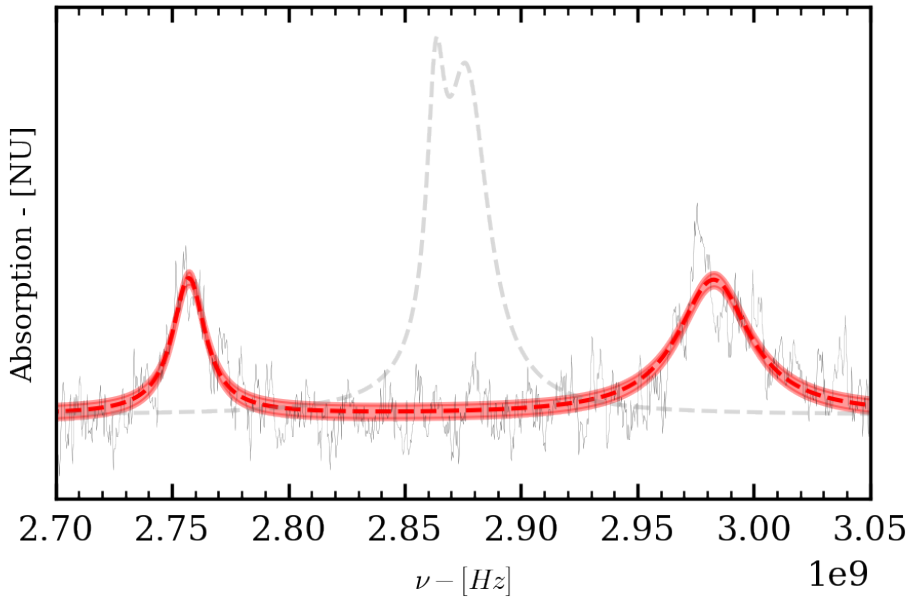

Figure 11: Magnetometry imaging of degeneracy lifting by Zeeman effect of the two sublevels $|1\rangle_{g,m_s=-1}$ and $|1\rangle_{g,m_s=+1}$. The resonant frequencies of RF-transitions are $D-\delta$ and $D+\delta$ under an external magnetic field. Here $2\delta \approx 225\ \ MHz$

Actually $\delta(\mathbf{B})$ has a complex dependence on $\mathbf{B}$, since only the projection of the magnetic field on the direction axis of the NV defect has a role. Given that there are only 4 possible directions for a defect, there are also 4 possible values of the frequency shift. If we denote $B_{i,i\in\{1,\dots,4\}}$ the four projections, the 4 possible frequency shifts write $\delta(B_i) = \delta_i$, $\forall i \in \{1,2,3,4\}$. Hence, 8 peaks should appear on the radiofrequency spectrum at points $\{D \pm \delta_i\}_{i\in\{1,2,3,4\}}$.

c Exploitation of the Zeeman effect

c.1 Data exploration For these peaks to be distinct, one needs to apply a strong magnetic field, ie. with $|\mathbf{B}| \gg |\mathbf{B}_{Earth}|$ or to change the projection of $\mathbf{B}$ on the four axis of the defects. Though the first way seems to be easier to conduct without changing our setup, we don't have access to sufficiently strong magnets. Our only alternative left is to change the projections of $\mathbf{B}$. For that, we fixed our magnet generating the external $\mathbf{B}$-field on a rotating support. By rotating the support we then change the orientation of $\mathbf{B}$ (knowing the magnetic contour lines) and consequently its projection along the 4 defects axis. From this study we can retrieve a lot of information, such as the orientation of the diamond sample, the value of numerous constant of (2) ... Results are shown on Fig.12.

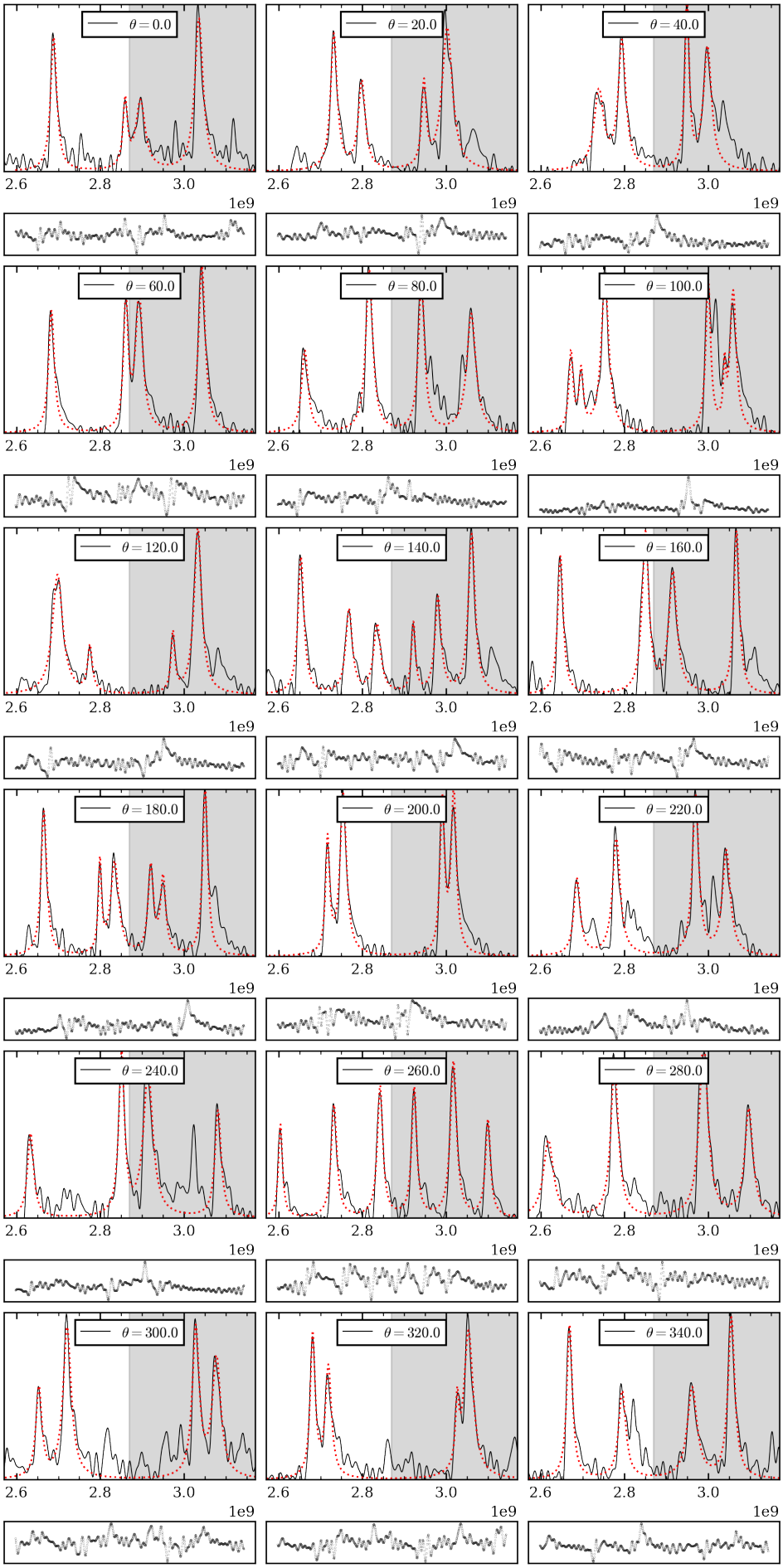
θ = 0.0
θ = 20.0
θ = 40.0
θ = 60.0
θ = 80.0
θ = 100.0
θ = 120.0
θ = 140.0
θ = 160.0
θ = 180.0
θ = 200.0
θ = 220.0
θ = 240.0
θ = 260.0
θ = 280.0
θ = 300.0
θ = 320.0
θ = 340.0
2.6
2.8
3.0
1e9

Figure 12: Magnetometry imaging (Absorbance over frequency [Hz]) of degeneracy lifting by Zeeman effect of the two sub-levels $|1\rangle_{g,m_s=-1}$ and $|1\rangle_{g,m_s=+1}$ for numerous orientations of the Magnetic field. The red curves are the Lorentzian fit of the peaks, and in black the raw signal. The sub-graphs are the residuals of the fit.
For this work we developed a library for finding and fitting all the Lorentzian peaks in the spectrum, with respect to the symmetric considerations (This is why some spikes in the spectrum are dropped, because they do not satisfy the symmetry requirements). The idea, behind this great data *mining* is to track the frequency shift of all peaks pair, in order to see what distribution they obey.

c.2 Projections in a tetrahedron Let's recall that the diamond structure is tetrahedral. One interesting thing about this structure, is the following: the distribution of the projections of a vector on the four axis of a tetrahedron is quite particular and not uniform. Then, the distribution of the frequency split (2) which depends on the projections should also be particular and distinguishable. Hence, studying this distribution regarding a fixed plane of projections, allows us to find the structural axes of the tetrahedron.

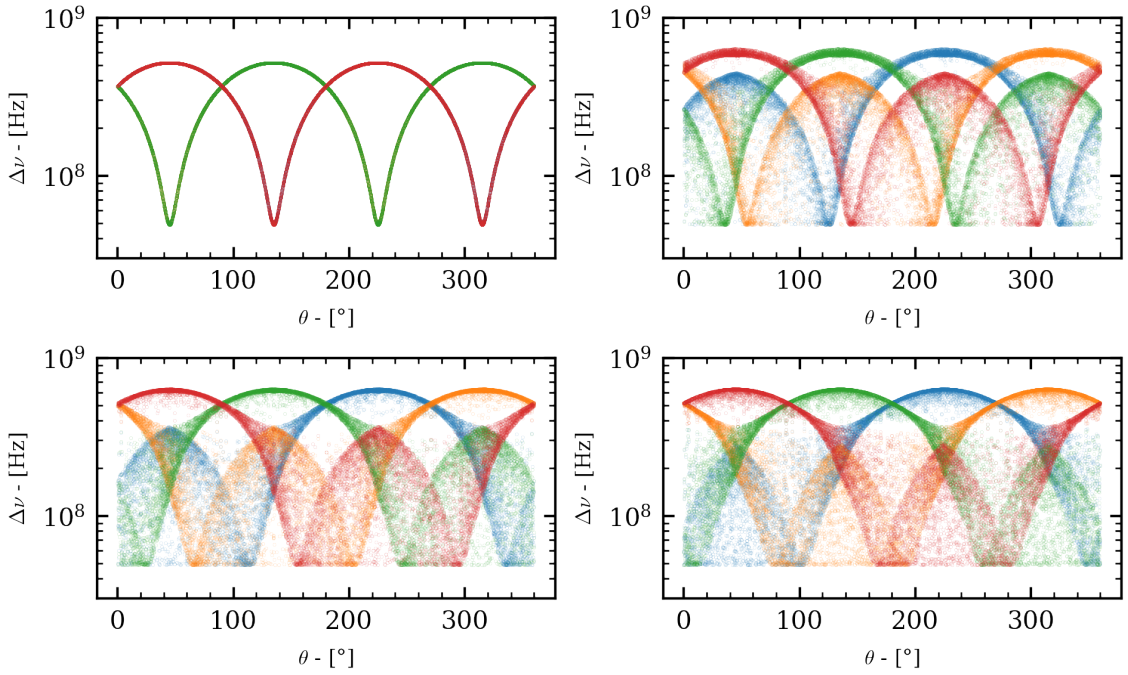

Figure 13: Here we take about 10000 projections on the 4 axes of the tetrahedron for 4 different 2D planes in space, one can see that there is different behaviours regarding, the number of different projections, and the distribution shape

The idea behind this is to see how many projections there are in our samples of data, one can remark, that there is often 2 values, and sometimes 3 of frequency shift. This means that the plane where we rotate our magnetic field $\vec{B}$ seems parallel to the plane parallel to one edge of the tetrahedron including the barycentre of the tetrahedron. This corresponds to the first distribution of the Fig.13.

c.3 Frequency split distribution study Now that we have determined the distribution to base our study, we can unearth the orientation of the diamond with the following : After determining the relative plane of $\vec{B}$ displacement, we can deal with angle issues since it is a 2d case. After retrieving all the frequency shifts for all angles, we obtain the following plots.

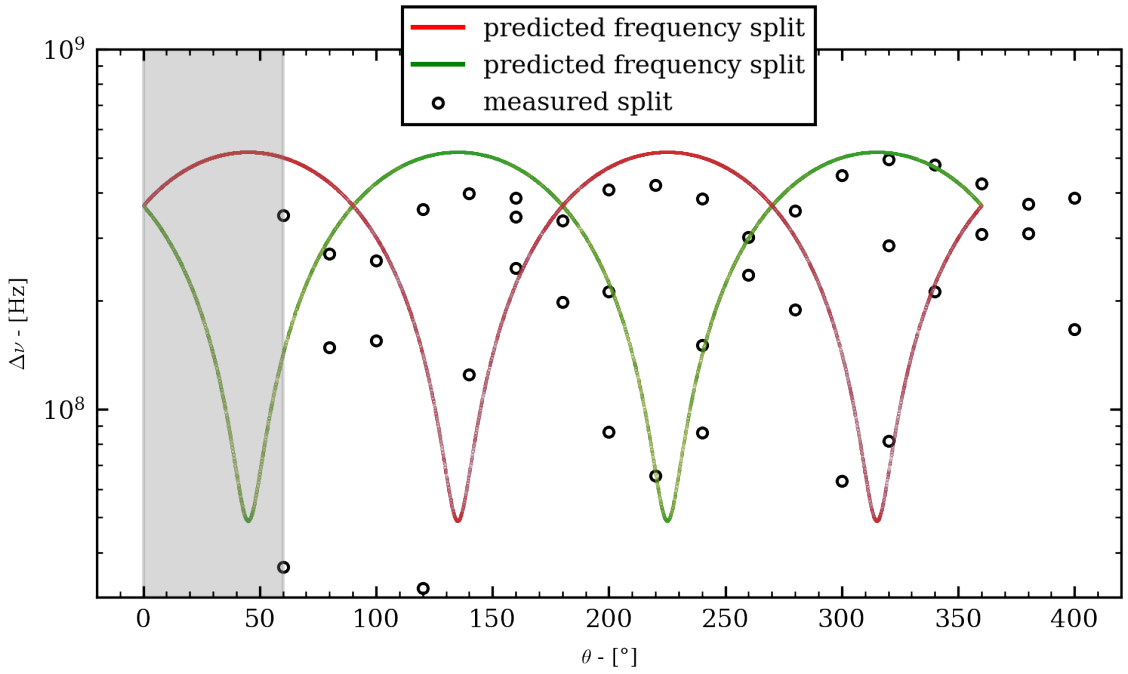

Figure 14: Predicted frequency distribution and measured shift. it appears that the best match with a 90 degree invariance is an angle of 60 degrees, for superposing the distribution and the samples. W cannot use a simple fit to find this angle, and must restrict ourselves to a simple visual inspection, these is why this measures must be taken with a grain of salt. However, let's note that the matching seems quite relevant.

c.4 Results It leads to the following conclusion: the horizontal plane (the plane where we are rotating $\vec{B}$) is parallel to one of the plane parallel to one edge of the tetrahedron of the tetrahedron including the barycentre of the tetrahedron, and the orientation of one axes of the tetrahedron is 60 degree z-rotation of the original tetrahedron defined by the following points : [1,1,1], [1,-1, -1], [-1, 1, -1], [-1,-1, 1].

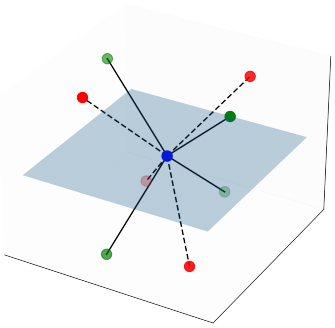

Figure 15: Visualizations of the tetrahedron orientation, in blue the plane of study, in green the original tetrahedron and in red the actual orientation in the diamond

Hence, we see that our sample has a strong dependence on **B** such as on its projections along the defects axis. This can be exploited in magnetometry for detection and imaging of weak magnetic field at the nanoscale. The sensing spins' wave function can be localized over only few lattice sites, providing this high spatial resolution, and quantum coherence of the spin yields high magnetic field sensitivities. NV centers can thus be used as nanoscale quantum sensors and scanning probes. This

is usually called nitrogen-vacancy magnetometry.

V Conclusion and Prospectus

In this study, we have conducted a thorough investigation into the behavior of nitrogen-vacancy (NV) centers in diamond, employing a combination of experimental techniques and rigorous data analysis. Our research focused on understanding the modulation of NV center signals, characterization of characteristic timescales, and exploration of the Zeeman effect on NV center behavior. Initially, we explored different modulation techniques, including internal and external modulation, to manipulate NV center signals. Despite encountering challenges such as signal triggering and amplitude modulation issues, our systematic approach allowed us to gain valuable insights into the modulation process and its limitations. Characterization of characteristic timescales proved to be pivotal in understanding the dynamics of NV centers. Through the use of burst mode techniques, we were able to precisely control exposure times and measure relaxation and excitation timescales. The measurement of AOM and photodiode rise-times provided essential information about experimental constraints, enabling more accurate interpretation of results. Furthermore, our investigation into the Zeeman effect on NV centers yielded significant findings. By carefully varying external magnetic fields and analyzing frequency shift distributions, we uncovered the complex behavior of NV centers in magnetic fields. The observed frequency shifts and their dependence on magnetic field projections provided crucial insights into the orientation and behavior of NV centers in diamond. Finally NV centers in diamond offers great opportunities, from nanoscale sensing to quantum information processing, and offer exciting possibilities for further exploration and development in the realm of diamond-based quantum technologies.

References

[1] Amanda Barnard. Diamond standard in diagnostics: Nanodiamond biolabels make their mark. *The Analyst*, 134:1751–64, 10 2009.

[2] A. Gruber, Alexander Dräbenstedt, C. Tietz, Fleury Ludovic, Joerg Wrachtrup, and C. Borczyskowski. Scanning confocal optical microscopy and magnetic resonance on single defect centers. *Science*, 276:2012–2014, 06 1997.

[3] F. Jelezko and J. Wrachtrup. Single defect centres in diamond: A review. *Physica Status Solidi Applied Research*, 203(13):3207–3225, October 2006.

[4] T. D. Ladd, F. Jelezko, R. Laflamme, Y. Nakamura, C. Monroe, and J. L. O'Brien. Quantum computers. *Nature*, 464(7285), March 2010.

[5] L Rondin, J-P Tetienne, T Hingant, J-F Roch, P Maletinsky, and V Jacques. Magnetometry with nitrogen-vacancy defects in diamond. *Reports on Progress in Physics*, 77(5):056503, may 2014.

[6] Romana Schirhagl, Kevin Chang, Michael Loretz, and Christian L. Degen. Nitrogen-vacancy centers in diamond: Nanoscale sensors for physics and biology. *Annual Review of Physical Chemistry*, 65(1):83–105, 2014. PMID: 24274702.